Velocity Distributions for Low Pressure Turbines

J. D. Coull

R. L. Thomas

H. P. Hodson

Whittle Laboratory,
University of Cambridge,
Cambridge CB3 0DY, UK

A parametric set of velocity distributions has been investigated using a flat-plate experiment. Three different diffusion factors and peak velocity locations were tested. These were designed to mimic the suction surfaces of low pressure (LP) turbine blades. Unsteady wakes, inherent in real turbomachinery flows, were generated using a moving bar mechanism. A turbulence grid generated a freestream turbulence level that is believed to be typical of LP turbines. Measurements were taken across a Reynolds number range 50,000–220,000 at three reduced frequencies (0.314, 0.628, and 0.942). Boundary layer traverses were performed at the nominal trailing edge using a laser Doppler anemometry system and hot films were used to examine the boundary layer behavior along the surface. For every velocity distribution tested, the boundary layer separated in the diffusing flow downstream of the peak velocity. The loss production is dominated by the mixing in the reattachment process, mixing in the turbulent boundary layer downstream of reattachment, and the effects of the unsteady interaction between the wakes and the boundary layer. A sensitive balance governs the optimal location of peak velocity on the surface. Moving the velocity peak forward on the blade was found to be increasingly beneficial when bubble-generated losses are high, i.e. at low Reynolds number, at low reduced frequency, and at high diffusion factors. [DOI: 10.1115/1.3192149]

1 Introduction

The flow inside turbomachinery turbine blade passages is inherently unsteady. Each blade row sheds turbulent wakes, which periodically convect through downstream passages. In addition, the freestream turbulence between these periodic wakes is also relatively high, being typically 3–6% [1]. The unsteady wakes and the turbulence have been shown to have a large impact on transition on turbine suction surface boundary layers [2].

In high aspect ratio low pressure (LP) turbines, the chord-based Reynolds numbers are relatively low. They are typically between 100,000 and 250,000 for a large civil engine at cruise, so large portions of the boundary layer tend to be laminar. This is of particular importance for suction surface boundary layers, which typically contribute between 60% and 85% of the profile loss [3,4].

Often, under steady flow conditions, the suction surface of a LP turbine blade has a laminar separation bubble and the flow undergoes transition in the separated shear layer, reattaching as a turbulent boundary layer. In the actual turbine, incoming wakes periodically cause early transition, shortening the bubble or even suppressing it entirely [2]. This can have a large effect on the development of profile loss. High-lift blade designs take advantage of the inherently unsteady environment (e.g., Ref. [5]) to control the transition of the suction surface boundary layer and therefore the loss. Consequently, manufacturers have benefited from a reduction in blade count and overall LP turbine weight.

Experimental modeling of the unsteady boundary layer interaction using cascades and flat plates has been crucial to our understanding of the flow behavior and the development of improved high-lift designs. Early studies without unsteady wakes include the work of Sharma et al. [4], who used a flat-plate experiment to compare two candidate velocity distributions for LP turbine suction surfaces. Measurements were carried out at high Reynolds number (~800,000) and the design with the furthest aft peak velocity was found to have the lowest loss.

Early work on simulating the interaction of periodic wakes with boundary layers was carried out using a rotating cage of bars upstream of a flat plate by Pfeil et al. [6], who identified periodic early transition induced by the passing wakes. Moving-bar mechanisms have been used in several experiments to simulate wakes, for example, the cascade work of Curtis et al. [3] and Stieger and Hodson [7].

Howell et al. [5] used a moving bar mechanism and a cascade of high-lift blades to examine a large range of suction surface velocity distributions. Boundary layer measurements were performed close to the trailing edge (TE), and the results suggested that moving the velocity peak further aft would reduce the loss. This work formed the basis for an improved cascade design, which proved to have 15% higher lift and yet a comparable loss to the datum high-lift blade.

Haselbach et al. [8] compared high-lift and ultra-high-lift blades in a three-stage LP turbine. The efficiency of the ultra-high-lift turbine was found to be the same as the high-lift design for an average blade Reynolds number of 210,000 but 0.5% less at a typical cruise Reynolds number of 90,000. Other examples of on-going experimental work comparing high-lift and ultra-high-lift cascades with periodic wakes include Refs. [9,10].

The primary aim of this study is to examine in detail the effects of changing the velocity distribution of the suction surface. A parametric set of velocity distributions has been imposed on a flat plate to investigate the effect of peak velocity location, diffusion factor (DF), and reduced frequency on performance and boundary layer behavior. A moving bar mechanism generated unsteady wakes and a turbulence grid was used to elevate the freestream turbulence level to 3.0%. Three normalized wake passing frequencies (0.314, 0.628, and 0.942) were investigated across a range of Reynolds numbers (50,000–220,000).

2 Experimental Methods

The experimental setup consists of a flat plate with moving bars, as presented in Fig. 1.

2.1 Test Section. The test section is designed to model the suction surface boundary layer of turbomachinery blades using a flat plate. The required velocity distributions were imposed by using sets of symmetric liners. The main design parameters are

Contributed by the International Gas Turbine Institute of ASME for publication in the JOURNAL OF TURBOMACHINERY. Manuscript received July 14, 2008; final manuscript received March 26, 2009; published online April 27, 2010. Review conducted by David Wisler. Paper presented at the ASME Turbo Expo 2008: Land, Sea and Air (GT2008), Berlin, Germany, June 9–13, 2008.

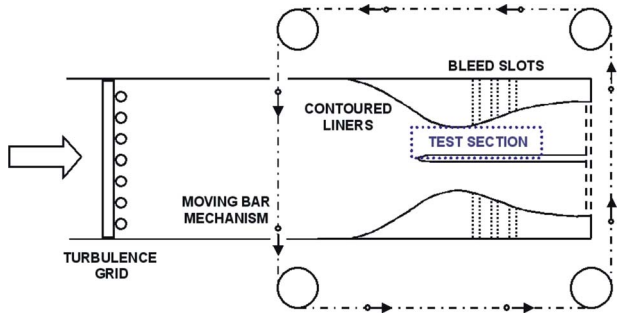

Fig. 1 Schematic of the flat-plate experiment

summarized in Table 1. The aluminum flat plate is 738 mm long, 458 mm wide, and 12.8 mm thick. For this work, the nominal trailing edge was fixed at a chordwise distance of 500 mm from the leading edge (LE). The leading edge is elliptical, with a semimajor axis of 38 mm. Eleven static tappings uniformly distributed around the ellipse were used in setting the incidence to zero. Incidence was controlled by independently adjusting the blockage at the exit of the top and bottom sections. 33 static pressure tappings (0.3 mm diameter) and 16 hot films are distributed along the length of the plate. These were placed at 40% and 60% of the span, respectively.

The total pressure was measured close to the leading edge. The exit static pressure was measured on the plate surface at the nominal trailing edge, at a chordwise distance of 500 mm from the leading edge.

A turbulence grid was installed upstream of the test section to generate a freestream turbulence level of 3.0% at the leading edge. Using a hot-wire measurement, the integral length scale Λ was calculated to be 37 mm using the autocorrelation function, so that

Table 1 Specification of flat-plate test rig with moving bars, with equivalent cascade parameters

Suction surface length S_0 (from stagnation point)	mm	502
Span	mm	458
Plate thickness	mm	12.8
Semimajor axis of elliptical LE	mm	38
Bar diameter	mm	7.8
Axial distance: bars to LE	mm	465
Bar pitch	mm	480 720 1440
Overall velocity ratio (inlet/exit)		1.87
Inlet freestream turbulence intensity		3%
Turbulence integral length scale Λ	mm	37
Equivalent chord C	mm	376
Equivalent axial chord C_x	mm	306
Equivalent trailing edge thickness t	mm	6.6
Reduced frequency $f_r = \left(\frac{f_{\text{bar}}C}{U_{\text{TE}}}\right)$		0.942 0.628 0.314

$$\Lambda = U\int_0^\infty R(\tau)d\tau \tag{1}$$

The overall velocity ratio between the inlet and the nominal trailing edge was 1.87. The Reynolds number Re_c was varied between 50,000 and 220,000, corresponding to trailing edge velocities of 2–8.5 m/s.

2.2 Equivalent Cascade Parameters. In order to relate the flat-plate results to those of an equivalent blade, the T106-series of high-lift turbine blades was used as a reference. The equivalent cascade parameters are included in Table 1. Previous studies of unsteady transition on these blades include the work on T106A carried out by Stieger and Hodson [7] and Opoka and Hodson [11], and the work on T106C carried out by Zhang and Hodson [12]. The T106C suction surface distribution is very similar to design A (see below), having a diffusion factor of 36% and peak velocity located at 42% of the surface length.

The Reynolds number (Re_c) and reduced frequency f_r are based on an equivalent chord, obtained using the ratio of surface length to chord from the T106-series. Strictly this is not correct because higher lift blades will tend to be more cambered and hence have a slightly higher ratio of surface length to chord, but it is sufficient for the purposes of this paper. Although Re_c is more commonly used, the fundamental Reynolds number controlling the boundary layer is the surface length-based Re_{S_0}. This can be obtained by multiplying Re_c by the ratio of surface length to chord, 1.34.

The reduced frequency f_r is defined by

$$f_r = \frac{f_{\text{bar}}C}{U_{\text{TE}}} \tag{2}$$

The reduced frequency describes the regularity of wake interactions. Variations can have a large effect on the loss generation mechanisms within the boundary layer. In a real LP turbine, this parameter will vary significantly with each stage due to the variations in the number of blades in each row, typically varying between 0.4 and 1. In the current study, reduced frequencies of 0.314, 0.628, and 0.942 were tested, with a minimum bar frequency of 1.4 Hz and a maximum of 20.5 Hz.

2.3 Velocity Distributions. Symmetric, contoured liners above and below the flat plate were used to impose a set of eight[1] velocity distributions on the surface. These were designed to obtain a parametric set of velocity distributions on the flat plate, allowing a systematic and controlled variation between three diffusion factors and three peak velocity locations. Bleed slots were cut into the contoured surfaces to avoid separation on the liners. These are indicated in Fig. 1. It was found that the degree of bleed flow required to maintain the diffusion factor changed slightly across the Reynolds number range. Therefore, a pair of sliding perforated sheets mounted over the exit to the test section were used to raise the pressure in the test section and gain greater control over the bleed rate.

Table 2 summarizes the eight velocity distributions, alongside the T106A data from Refs. [13,14] and the T106C data from Ref. [15] for comparison.

2.4 Measurement Techniques and Data Reduction. The pressure measurements were taken with a Scanivalve DSA 3017 16 channel pressure scanner with a range of 2500 Pa and a 0.125 Pa resolution. Pressure measurements along the length of the plate were acquired using a 48 port Scanivalve multiplexer coupled to a single channel of the DSA pressure scanner. The pressure differences with respect to the inlet total pressure were in the range 3–30 Pa.

[1]The ninth design (DF=40%, S_{peak}/S_0=62%) was found to exhibit high levels of secondary flow so has not been measured.

Table 2 Summary of designs tested. Steady separation and reattachment locations have been derived from low reduced frequency hot-film measurements. T106A and T106C data from Refs. [11,12].

Design	Diffusion factor (%)	Peak velocity location ($\%S_0$)	Zweifel lift coefficient	Pitch: chord ratio	Steady state locations ($Re_c \approx 130{,}000$)	
					Separation ($\%S_0$)	Reattachment ($\%S_0$)
A	40	42	1.18	0.950	52	70
B	40	52	1.16	0.931	59	74
C	28	42	1.09	0.874	54	79
D	28	52	1.06	0.855	59	83
E	28	62	0.996	0.802	68	88
F	16	42	0.978	0.788	54	98
G	16	52	0.960	0.773	59	96
H	16	62	0.919	0.740	68	96
T106A	22	45	1.05	0.798	60	-
T106C	36	42	1.15	0.96	50	74

A two-dimensional Dantec laser Doppler anemometry (LDA) system was used to perform boundary layer traverses at the nominal trailing edge. A total of 17 points were measured in the traverse.

The LDA system included a 5 W argon ion laser (Coherent Innova 90C) and a Dantec FiberFlow System with a beam expander. A back-scatter setup was used. The size of the measuring volume was approximately $0.08 \times 0.08 \times 1.00$ mm^3. Data were collected in dead time mode. The data acquisition rate varied between 0.5 kHz and 5 kHz. A minimum of 200,000 data points was collected at each traverse location.

Seeding for the LDA measurements was provided using a TSI Six Jet Atomizer with Shell Odina oil. Smoke was injected through the trailing edge of an aerofoil shaped section positioned approximately 6 m upstream of the test section. This system gives a mean particle size of approximately 1.5 μm.

The postprocessing of the LDA data used a coincidence filter. The velocity bias inherent in LDA measurements was removed using a residence time weighting factor defined in [16]

$$\eta_i = \frac{t_{ri}}{\sum_{j=1}^{N} t_{rj}} \tag{3}$$

The LDA data were phase averaged with respect to the wake passing period. The wake period is divided into 128 time bins and the recorded bursts allocated to each time bin accordingly, weighted by the respective residence time weighting factor. The phase-averaged velocity was then calculated according to

$$\langle u \rangle = \sum_{i=1}^{N} \eta_i u_i \tag{4}$$

Surface mounted hot-film sensors were used to measure the wall shear stress in a semiquantitative manner. The so-called quasi-wall shear stress [17] is given by

$$\tau_w = \left(\frac{E^2 - E_0^2}{E_0^2} \right)^3 \tag{5}$$

where E is the hot-film bridge output velocity and E_0 is the value of E at zero-flow conditions. This method of data reduction allows the relative magnitude of the shear stress to be compared between sensors, without the need for elaborate calibration of the sensors. Hot-film measurements were obtained at three Reynolds numbers for each design and reduced frequency. The data were logged at a frequency of 20 kHz and 256 ensembles were recorded for several wake passing periods.

Oil-and-dye flow visualization was used for each velocity distribution to ensure the flow was largely two dimensional, without significant secondary flow effects. To minimize the effects of the sidewalls, the boundary layers were bled off upstream of the test section and trip wires were used to induce early transition, hence preventing the sidewalls separating in the diffusing section. The flow visualization technique also allowed observation of the boundary layer separation and reattachment locations for each setup.

2.5 Processing of Results

2.5.1 Circulation, Pitch-to-Chord, and Zweifel Coefficient. The circulation for each velocity distribution was calculated from the measured suction-side velocity distributions and assumed pressure-side distributions, using

$$\text{circulation} = \oint U \cdot dS \tag{6}$$

The pressure surface distributions were based on the T106-series of cascades. Designs A and B, having a diffusion factor of 40%, were assumed to have the pressure surface distribution of T106C, which has a suction surface diffusion factor of 36% [13]. Designs F–H, having a diffusion factor of 16%, were assumed to have the pressure surface distribution of T106A, which has a suction surface diffusion factor of 21% [14]. The pressure surface distribution of Designs C–E, having a diffusion factor of 28%, were assumed to be an average of both T106A and T106C.

Figure 3 shows the three pressure surface velocity distributions together with each measured suction surface velocity distribution. Published cascade measurements of surface velocity for the T106A and T106C blades have been plotted in Fig. 2 for comparison.

The pitch-to-chord ratio for each design was calculated from the circulation and the T106C design inlet and exit flow angles (32.7 deg and 63.2 deg, respectively [12].

The Zweifel lift coefficients were calculated for each design, using the pitch-to-chord ratio, the T106 axial chord, and the assumed inlet and exit flow angles. Equation (7) defines the relationship.

$$Z = \frac{s}{C_x} \left(\frac{\tan \alpha_2 - \tan \alpha_1}{0.5 \sec^2 \alpha_2} \right) \tag{7}$$

2.6 Loss Calculation. Boundary layer profiles at the nominal trailing edge, obtained using the LDA traverses, were used to calculate the boundary layer integral parameters. These measurements were converted to an equivalent blade row loss for a cascade with uniform exit velocity. The suction surface contribution

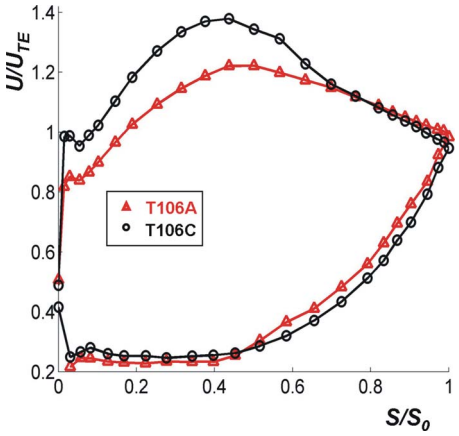

Fig. 2 Measured surface velocity for T106A [14] and T106C [15]. $Re_c \approx 210{,}000$, $f_r \approx 0.6$, and $Tu \approx 4\%$.

to loss was calculated based on the following expression for the pressure loss coefficient in a blade passage as presented by Denton [18]:

$$\zeta = -\left(\frac{C_{pb}t}{s\cos(\alpha_2)}\right) + \left(\frac{2\theta}{s\cos(\alpha_2)}\right) + \left(\frac{\delta^* + t}{s\cos(\alpha_2)}\right)^2 \quad (8)$$

The three terms in this equation represent the base pressure loss, the momentum deficit loss and the blockage loss respectively. The base pressure was not measured and so the loss due to the first term cannot be estimated for this flat-plate setup. Previous work has suggested that the base pressure can slightly reduce the loss for high-lift blades [19,3] and its effects are typically small. The suction surface loss coefficient was therefore calculated using the remaining momentum deficit and blockage terms in Eq. (8). The momentum deficit term dominates, typically being around 100 times larger than the blockage term in the current measurements.

A Thwaites calculation for the (assumed laminar) pressure-side boundary layers was used to determine an estimate of the pressure-side loss contribution at each Reynolds number. Typical pressure-side loss contributions were between 9% and 15% of the total loss, being higher for the low-lift designs and varying only slightly ($\pm 1\%$) with changing Reynolds number. These calculations were not included in the final loss results.

In real turbomachines, aft-loaded high-lift turbines can have a large amount of uncovered turning over the aft portion of the blade. Consequently the freestream velocity at the trailing edge (which is the exit velocity in the current experiments) will be lower than the mean exit velocity. The difference can be up to 5%. Equation (8) will therefore tend to overpredict the loss with respect to the real performance.

2.6.1 Intermittency. The proportion of time for which a transitional boundary layer is turbulent is defined as the intermittency. Turbulent flow can be identified in thermal anemometry measurements as regions of high-frequency fluctuations.

An intermittency detection routine was developed for the analysis of the hot-film data. This used a combined threshold and peak-valley-counting method based on Ref. [20]. The threshold levels and window sizes for each hot-film sensor and measurement were adjusted manually to account for variations in signal amplitude across the array. Further details and background on intermittency detection can be found in Ref. [20].

2.6.2 Uncertainty Analysis. Estimates of the errors in the measurements were obtained by considering the primary sources of inaccuracy.

It was evident from the time variation of the phase-averaged velocity $\langle u \rangle$ that there was a small amount of noise in the data, typically less than 0.05 m/s per time bin. To quantify the effect on the boundary layer integral parameters, small random errors were superimposed onto a sample velocity profile and the boundary layer integral parameters then evaluated. This was repeated numerous times across a range of freestream velocities to obtain a statistical estimate of the error in the loss measurements. It was found that at all Reynolds numbers, a small bias error was introduced and the loss tends to be overestimated by 2% of the total value.

The diffusion factor for each profile was controlled by adjusting the bleed flow. Hence, errors in the pressure measurements can change the diffusion factor of each setup. This is of particular concern at low Reynolds number where the dynamic pressures are low. This is because the measurements show that an increase in the diffusion factor tends to increase the loss. An empirical relationship between the loss and the diffusion factor at different Reynolds numbers was used to translate the anticipated error in the diffusion factor into an error in the measured loss.

The estimated errors in the losses are shown in Fig. 5 as vertical bars.

2.7 NGTE Boundary Layer Code. A boundary layer code was used to provide comparisons with the experiments. The National Gas Turbine Establishment (NGTE) code uses integral methods to calculate boundary layer parameters for a specified velocity distribution. It is described in detail by Herbert and Calvert [21]. The laminar portion of the boundary layer is calculated using an adaptation of the Thwaites method. Transition onset is calculated either by the attached flow correlations of Abu-Ghannam and Shaw [22] or separated flow correlations based on Ref. [23]. It can also be specified. The turbulent portion of the boundary layer is calculated using the lag-entrainment method outlined by Green et al. [24].

3 Discussion of Results

3.1 Surface Velocity Distributions. The measured velocity distributions for all eight designs are shown in Fig. 3. In each case, the flow accelerates over the front portion of the surface up to the peak velocity location, remaining laminar. As the flow decelerates downstream of this point, the boundary layer always separates. This is visible as a slight deviation in the velocity distribution, shown, for example, between $60\%S_0$ and $75\%S_0$ for design D in Fig. 3(*b*). Transition then occurs in the separated shear layer, which subsequently reattaches as a turbulent boundary layer. This is indicated by the rapid drop in velocity, as seen between $75\%S_0$ and $85\%S_0$ for design D.

Profiles E and H have reduced leading edge loading compared with the other designs and consequently have lower lift coefficients than their more forward loaded equivalents. This has a small effect on the losses, which will be discussed in more detail in Sec. 3.3.2.

3.2 Results for Design D. The velocity distribution D lies in the middle of the parameter space, having a diffusion factor of 28% and peak velocity located at $52\%S_0$. This design will be used to provide a description of the general flow.

3.2.1 Reynolds number = 127,000, $f_r = 0.628$. Figure 4 shows a space-time diagram of measured hot-film and LDA data for design D at $Re_c = 127{,}000$ and $f_r = 0.628$. Three wake passing periods have been plotted. The ensemble-averaged quasi-wall shear stress, obtained from hot-film measurements, is represented by the flood contours, with line contours of ensemble-averaged intermittency (in steps of 0.1) superimposed. The streamwise positions of each hot-film sensor have been indicated by white dots along the top of the diagram. The quasi-wall shear stress values drop sharply as the flow diffuses, reaching low values in the separation bubble and remaining low until flow reattachment. To the side, the time variation of momentum thickness at the trailing edge has been plotted, with an approximate steady flow value represented by the vertical

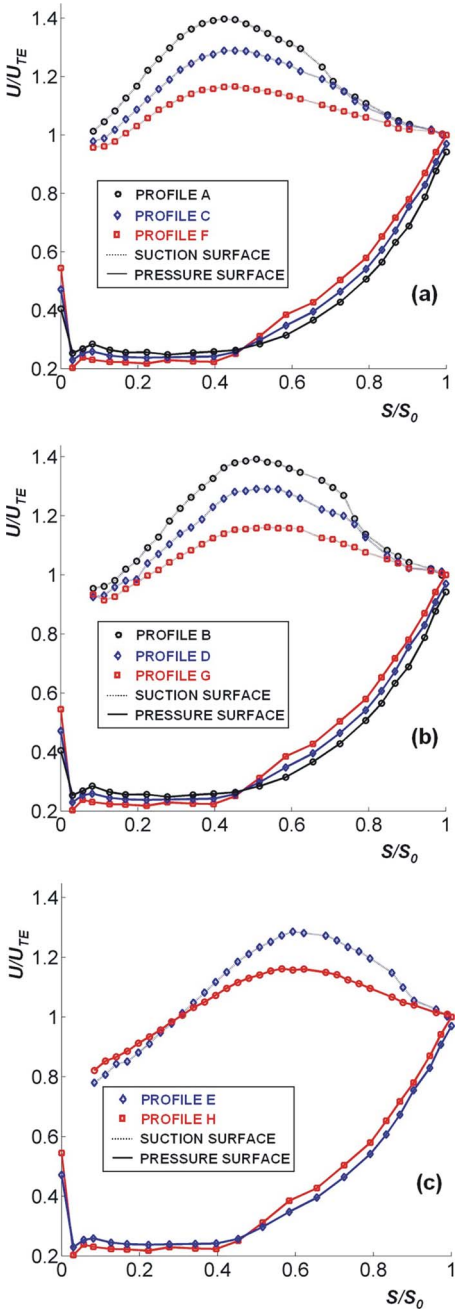

Fig. 3 Measured surface velocity for all velocity distributions tested (Re_c=200,000 and f_r=0.628) with assumed pressure-side distributions for each

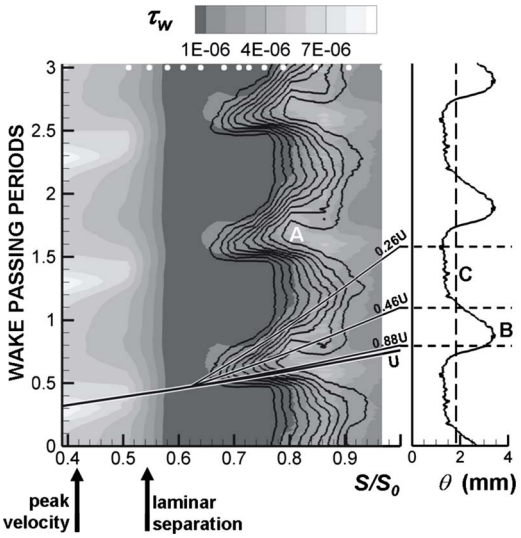

Fig. 4 LHS: Space-time plot for design D for Re_c=127,000 and f_r=0.628. Flood contours of quasi-wall shear stress, line contours of intermittency (in steps of 0.1). RHS: Trailing edge momentum thickness variation.

dashed line. This was estimated using the measurements obtained at the lowest reduced frequency for the same design and Reynolds number, where a steady value of momentum thickness was evident between the wakes.

A line representing the measured freestream velocity U for design D has been superimposed along the centerline of the fluctuations in the quasiwall shear stress data in Fig. 4. The centerline of the convecting wake approximately follows this line. Three additional lines have been drawn, originating from the onset of wake-induced transition, corresponding to various proportions of the freestream velocity. The first two lines (88%U and 46%U) approximately indicate the leading and trailing edge velocities of the wake-induced turbulent region. These values were calculated using the average pressure gradient in the diffusing region of the boundary layer and the correlations for turbulent spots in adverse pressure gradients presented by Gostelow et al. [25]. The trailing edge velocity of the ensuing calmed region has also been marked (26%U). This was assumed to travel at the same fraction of the turbulent trailing edge velocity as for a zero-pressure gradient flow. The wedge formed by these lines indicates the approximate region of flow influenced by the wake-induced transition.

Under the wake path, as represented by line U, the intermittency contours in Fig. 4 show that the wake-induced transition begins around 65%S_0 and is almost complete by 80%S_0 (marked A on Fig. 4). Simultaneously, the quasiwall shear stress rises to a high value indicating reattachment of the separated boundary layer. Inspecting the momentum thickness variation between the 88%U and 46%U lines, marked B, one can see that this region of early transition is associated with a large increase in the trailing edge momentum thickness. This high loss immediately following the wake centerline cannot be accounted for by the early transition in the shear layer since it is known that this tends to reduce the loss. The origin of the extra loss is therefore not clear but one may postulate several possibilities. Mechanisms similar to the large-scale vortex shedding and subsequent mixing identified by Stieger and Hodson [7] will contribute to the loss production. Although the current measurements have not identified these structures, vortex shedding has previously been identified on the T106A and T106C profiles under similar conditions [11,12]. Another possible source of loss could be a thickening of the boundary layer due to the entrainment of low momentum wake fluid. Following behind the wedge of wake-induced turbulent flow in Fig. 4 is the calmed region (between the 46%U and 26%U lines). This is a region of laminar-like flow that resists separation. The separation bubble therefore continues to be suppressed after the passage of the wake, resulting in the reduction in loss evident in the low momentum thickness at the trailing edge after the passage of the wake (marked C), which has a value of only ~1.5 mm compared with the steady flow value of 1.9 mm.

The momentum thickness plot in Fig. 4 shows that at this reduced frequency, the influence of the calmed region is still apparent at the trailing edge when the next wake arrives. For lower reduced frequencies, a slow return to steady state can be observed before the arrival of the subsequent wake (this will be covered in Sec. 3.2.2).

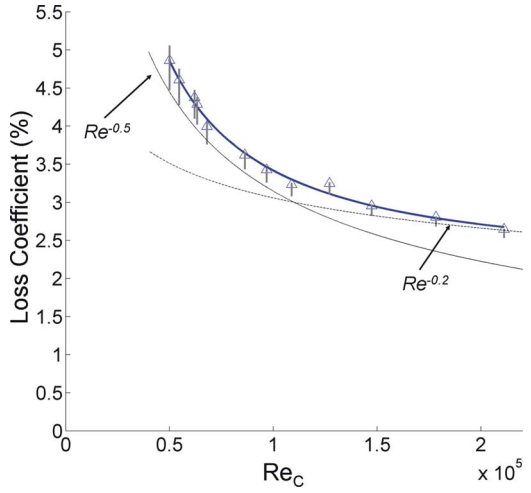

Fig. 5 Loss variation for design D at f_r=0.628 with error bars and curves of $Re_c^{-0.5}$ and $Re_c^{-0.2}$

Table 3 Steady flow bubble lengths and turbulent boundary layer lengths at three Reynolds numbers for design D

Re_c	Length of bubble ($\%S_0$)	Turbulent boundary layer coverage ($\%S_0$)
213,000	16	25
124,000	24	17
62,500	31	10

3.2.2 Variation of Loss With Reynolds Number. Figure 5 shows the measured suction surface loss coefficient for design D at f_r=0.628 across a range of Reynolds numbers, with estimated errors for each point represented by the gray vertical bars. A trend line has been fitted through the data points. Two further curves have also been plotted showing the trends governing laminar loss ($Re_c^{-0.5}$) and turbulent loss ($Re_c^{-0.2}$). The magnitude of these two curves has been arbitrarily chosen to enable comparison with the measurements.

With decreasing Reynolds number, the losses increase rapidly. For values below approximately Re_c=110,000, the loss values more closely follow the laminar loss trend, suggesting that the laminar flow dominates the production of loss in this Reynolds number range. The boundary layer losses upstream of separation are typically very low, implying that the mixing during the reattachment of the separation bubble is contributing greatly to the loss production.[2] Above Re_c=110,000, the curve starts to follow the turbulent loss trend, suggesting that in this region the losses generated in the turbulent boundary layer downstream of reattachment are beginning to dominate over the bubble-generated losses.

The steady-state boundary layer behavior at different Reynolds numbers helps to explain the trends seen. Table 3 lists the steady flow lengths of the bubble and the turbulent boundary layer at three Reynolds numbers. At the highest Reynolds number, where we see the loss curve closely following the turbulent trend, we can see that the bubble is small and the extent of the turbulent boundary layer is large (25% of the total surface length). As the Reynolds number decreases the bubble grows progressively larger and the extent of the turbulent boundary layer reduces. A larger bubble causes greater mixing of the boundary layer during flow reattachment and this intensifying process begins to dominate over the turbulent-generated losses. It is in this region that we see the loss curve in Fig. 5 more closely following the laminar trend.

[2]Although the flow is not laminar during reattachment, the mixing loss is dependant on the maximum displacement thickness of the bubble (see Ref. [28]), which will be governed by the laminar portion of the bubble.

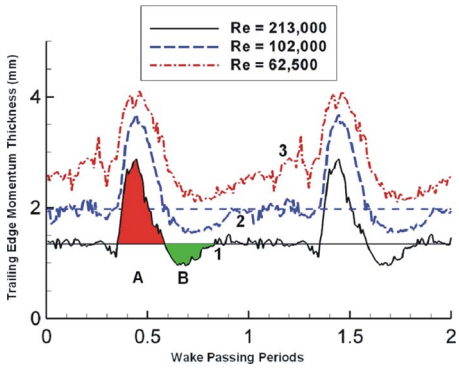

Fig. 6 Time variation of trailing edge momentum thickness for design D at f_r=0.314 for three Reynolds numbers, with estimated steady flow values

The influence of the unsteady wakes can also be seen to change with Reynolds number. Figure 6 shows the variation with time of trailing edge momentum thickness for the design D for f_r=0.314 at three Reynolds numbers. The data have been repeated for two wake passing periods. As the measurements presented in Fig. 5 show, the momentum thickness increases as the Reynolds number reduces. Figure 6 also shows that the influence of the calmed region extends in time as Reynolds number reduces. Points 1–3 mark the approximate end of each calmed region for the three cases presented.

For the two highest Reynolds number cases, Re_c=102,000 and 213,000, estimates of the steady flow momentum thickness have been plotted as horizontal lines in Fig. 6. These can be seen to pass through points 1 and 2. The net effect of each wake is to create the combination of the high-loss turbulent region followed by the lower-loss calmed region (shaded regions A and B, respectively). At the highest Reynolds numbers, the net effect of each wake is an increase in the momentum thickness relative to steady flow. This is because the separation bubble is small and the net effect of each wake (the combination of shaded regions A and B) is an increase in the overall loss. However, for the low Reynolds number case, Re_c=62,500, the influence of the low-loss calmed region continues to persist until the arrival of the subsequent wake at point 3. Here, the momentum thickness is still low and rising toward a steady value, indicating that the bubble does not have time to fully re-establish between wakes. The steady flow momentum thickness at this Reynolds number will therefore be greater than the value at point 3 (θ=3 mm). By considering the net effect of each wake (again as the combination of the high-loss turbulent and low-loss calmed region), it can be seen that the overall effect of each wake is to reduce momentum thickness compared with the steady flow value (from 3+mm to 2.8 mm). This shows that the wakes tend to reduce the loss at low Reynolds numbers and increase the loss at high Reynolds numbers.

3.2.3 Variation of Loss With Reduced Frequency. As discussed above, the unsteady wakes periodically reduce the extent of the separation bubble and therefore reduce the associated mixing losses. This is at the expense of the high-loss region that arrives at the trailing edge immediately following the centerline of each wake (area A in Fig. 6). At low Reynolds numbers, the introduction of wakes reduces the dominant bubble-generated losses, and hence a further increase in the wake passing frequency will tend to be beneficial. Conversely, at high Reynolds numbers, the bubble-generated losses are low and the benefit from the suppression of the bubble is small (area B in Fig. 6). The high-loss turbulent regions therefore cause an increase in the overall loss.

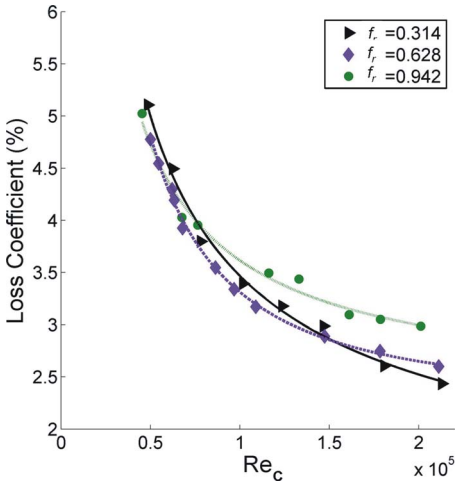

Fig. 7 Variation of loss coefficient with Reynolds number at three reduced frequencies for design D

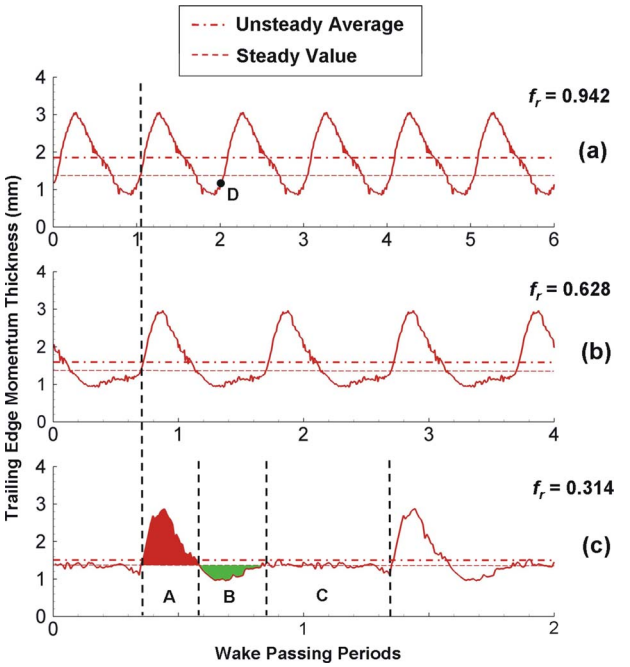

Fig. 8 Time variation of trailing edge momentum thickness for design D at Re$_c$≈210,000 and three reduced frequencies

Hence in general at high Reynolds numbers, an increase in the reduced frequency will tend to increase the loss. This trend is consistent with the high Reynolds numbers results used in the correlation of Hodson [26].

The balance between the sources of loss is evident in the variation of loss with reduced frequency, f_r, as shown for design D in Fig. 7. At high Reynolds numbers (Re$_c$ > 150,000), the bubble is small and the loss is dominated by the turbulent boundary layer. Increasing the wake passing frequency in this region causes the overall loss to rise. This was evident in Fig. 6, where each wake increased the loss relative to the steady flow case at high Reynolds numbers. At low Reynolds numbers, the bubble grows in size and provides a greater contribution to the overall loss. As the results in Fig. 6 imply, increases in the wake frequency for low Reynolds numbers are generally beneficial as the size of the bubble, and hence the amount of associated mixing, is reduced. Indeed, Fig. 7 shows that as the Reynolds number drops below 150,000, the higher reduced frequency (0.628) case has lower loss than the low reduced frequency (0.314) case. The data also suggest that the loss for the highest reduced frequency (0.942) will be lower than for the other frequencies below Re$_c$=50,000. One can quickly see from this behavior that the balance between bubble-generated and attached turbulent flow loss production mechanisms within the boundary layer needs to be determined to fully understand the impact of a change in reduced frequency.

Figure 8 shows the time variation of the trailing edge momentum thickness θ for design D at three reduced frequencies ((a) 0.942, (b) 0.628, and (c) 0.314) at Re$_c$≈210,000. One ensemble of data has been repeated for each case. For all three cases, the pattern of momentum thickness variation during and immediately following each wake event is almost identical.

Three distinct regions have been marked as A, B, and C on the low reduced frequency plot in Fig. 8(*c*). These correspond to the following:

A. the high-loss wake-induced turbulent region
B. the low-loss calmed region
C. quasi-steady flow between the wakes

Underneath each wake (A), the momentum thickness rises to a peak of approximately 3 mm, before dropping in the calmed region (B) to a minimum of 1.0 mm. Following the calmed region, the boundary layer returns to a steady value of 1.4 mm before the arrival of the subsequent wake. As observed in Figs. 6 and 7, the effect of each wake at this Reynolds number is to increase the loss relative to the steady flow value. Therefore, in the lower reduced frequency case, f_r=0.314 (Fig. 8(*c*)), the average momentum thickness increases slightly to 1.5 mm from the steady flow value of 1.4 mm. This increase in overall loss becomes more pronounced with increasing reduced frequency, such that for f_r =0.942 (Fig. 8(*a*)) the average momentum thickness rises to 1.84 mm. For this higher reduced frequency case, each wake arrives in the middle of the calmed region (at the point marked D in Fig. 8(*a*)). The would-be lower momentum thickness of the calmed region is replaced by an elevated level and hence much of the benefit of this region is lost. A similar argument was used by Lazaro et al. [27] to explain the variation of loss with reduced frequency.

3.3 Parametric Study of Velocity Distributions. The influence of velocity distribution design will now be discussed. From the examination of results in Fig. 5, it was found that the loss followed a laminar trend at low Reynolds numbers. It can be shown [29] that for a self-similar laminar boundary layer (such as the Falkner-Scan solutions) that

$$\mathrm{Re}_\theta = f\left(\frac{dU/U}{dS/S}\right)\mathrm{Re}_S^{1/2} \tag{9}$$

where Re$_\theta$ is the Reynolds number based on momentum thickness, Re$_S$ is the Reynolds number based on the surface distance S, and $(dU/U)/(dS/S)$ is the non-dimensional deceleration rate. This equation can be considered as

$$\mathrm{Re(loss)} = f(\text{deceleration rate}) \times \mathrm{Re(distance)}^{1/2} \tag{10}$$

This result highlights the potential importance of the non-dimensional deceleration rate $(dU/U)/(dS/S)$. The average value of this parameter for each of the designs tested is given by

$$\text{non-dimensional deceleration rate} = \frac{(\Delta U/U_{\mathrm{TE}})}{(\Delta S/S_0)} = \frac{DF}{1 - S_{\mathrm{peak}}/S_0} \tag{11}$$

which is equal to the diffusion factor $(\Delta U/U_{\mathrm{TE}})$ divided by the non-dimensional length of the decelerating region $(\Delta S/S_0)$, determined by the peak velocity location. The distance over which the flow is decelerated is determined either by the distance $\Delta S/S_0$ or by the total deceleration $(\Delta U/U_{\mathrm{TE}})$ (together with the deceleration

Table 4 Approximate bubble and turbulent boundary layer lengths for three designs with $S_{peak}/S_0=52\%$ for $Re_c \approx 130{,}000$

Design name	Diffusion factor (%)	Surface distances: Length of bubble ($\%S_0$)	Surface distances: Turbulent attached ($\%S_0$)	Average deceleration rate[a]
B	40	15	26	0.83
D	28	24	17	0.58
G	16	37	4	0.33

[a]Equation (11).

rate). Thus these two parameters are key to the generation of boundary layer momentum thickness and hence profile loss at a given Reynolds number.

3.3.1 Diffusion Factor Variation. Although desirable in terms of increasing the blade lift, increasing the diffusion factor also tends to increase loss production, as Eq. (9) suggests. As the diffusion factor rises, the velocities across the surface increase, the loss generated by the separation bubble tends to rise, and the turbulent wetted area increases. To a certain extent, the resulting increase in loss is mitigated by having fewer blades in the blade row.

The steady flow behavior of each boundary layer highlights the effect of changing the diffusion factor. Table 4 summarizes the steady flow lengths of the bubbles and the extent of turbulent flow (obtained from hot-film data) for three velocity distributions, which have the peak velocity located at $52\%S_0$ with varying levels of lift, design B (DF=40%), design D (DF=28%), and design G (DF=16%), at $Re_c \approx 130{,}000$. The average non-dimensional deceleration rate has been presented in the final column. As the diffusion factor and the deceleration rate increase, the bubble-generated losses will tend to rise. Transition and reattachment are also observed to move upstream,[3] thereby increasing the turbulent wetted area and hence the turbulence-generated losses. It can therefore be expected that loss will rise with increasing diffusion factor across the Reynolds number range.

Loss measurements for designs B, D, and G at a reduced frequency $f_r=0.628$ are shown in Fig. 9. Lines representing a laminar loss ($Re_c^{-0.5}$) and a turbulent loss ($Re_c^{-0.2}$) have been superimposed, as in Fig. 5. As expected, the loss increases with diffusion factor across the Reynolds number range, rising rapidly at the lowest Reynolds numbers.

Each design in Fig. 9 exhibits a different balance between the laminar trend, associated with the bubble-generated loss, and the turbulent trend, associated with the loss generated downstream of reattachment. The 16% DF design follows the turbulent $Re_c^{-0.2}$ trend for Reynolds numbers above approximately 90,000, below which the losses begin to increase more rapidly. This suggests that the bubble-generated losses for this design are very small and the turbulence-generated losses are the greatest contributing factor. As the diffusion factor and hence the deceleration rate increase, the losses increasingly appear to follow the laminar trend, indicating that bubble-generated losses dominate over contributions from the turbulent boundary layer, even though both increase.

To quantify the influence of the separation bubble, it is necessary to consider the other factors affecting the loss. We need to quantify the increase in loss due to the higher surface velocities at high diffusion factors and the effect of Reynolds number on losses

[3]The shortening of the separation bubble with increasing diffusion rate may at first seem nonintuitive. However, bubbles in highly decelerating flow will grow in height more quickly, promoting earlier breakdown into turbulence. Thus, transition and reattachment will tend to move upstream. It should also be noted that the loss produced by a separation bubble is not dependant on its length; rather it is the maximum height of the bubble which is important (see Ref. [28]).

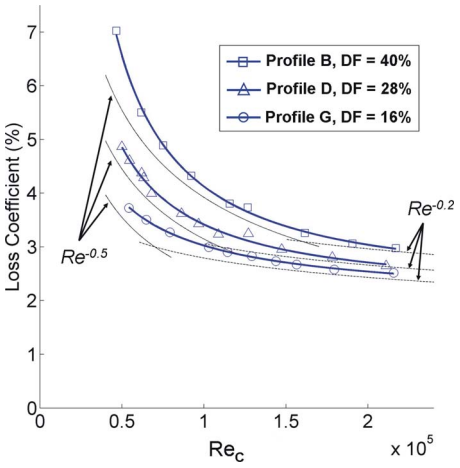

Fig. 9 Loss coefficient variation against Reynolds number at three diffusion factors. $S_{peak}/S_0=52\%$, and $f_r=0.628$.

generated in the laminar attached and turbulent regions of the boundary layer. To achieve this a comparison is made between the measured loss and the predicted loss of the boundary layers without the separation bubble. These predictions were obtained by using the NGTE integral method with transition specified at the separation point, which occurred at $59\%S_0$ for all three designs. Figure 10 shows the measured loss coefficient for designs B, D, and G for $f_r=0.628$ alongside the NGTE code predictions. The difference between these curves has also been plotted, representing an estimate for the unsteady bubble-generated losses of each design.

The NGTE predictions show an increase in loss with diffusion factor. However, at low Reynolds numbers, they do not exhibit the large increases in loss for the two higher diffusion factors, as seen in the measurements. The estimated unsteady bubble loss values therefore show that the bubble generates more loss as the diffusion factor increases, and that this increase becomes more severe at low Reynolds numbers.

The measurements from all eight designs were compared with a study of different velocity distributions presented by Curtis et al. [3]. The work of Curtis et al. [3] was carried out on a moving bar cascade. A variable trailing edge flap and passage inserts were used to alter the suction surface velocity distribution. The

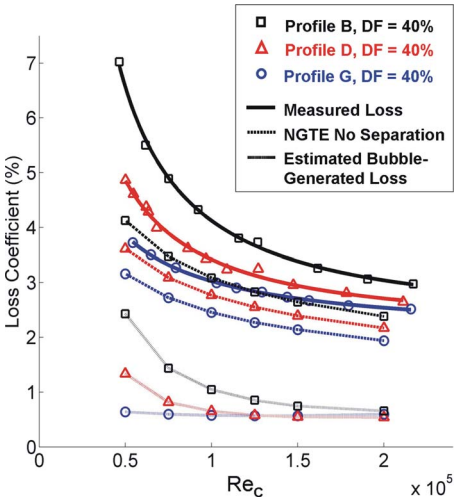

Fig. 10 Comparison of measured loss coefficients for $f_r=0.628$ against non-separated NGTE boundary layer calculations.

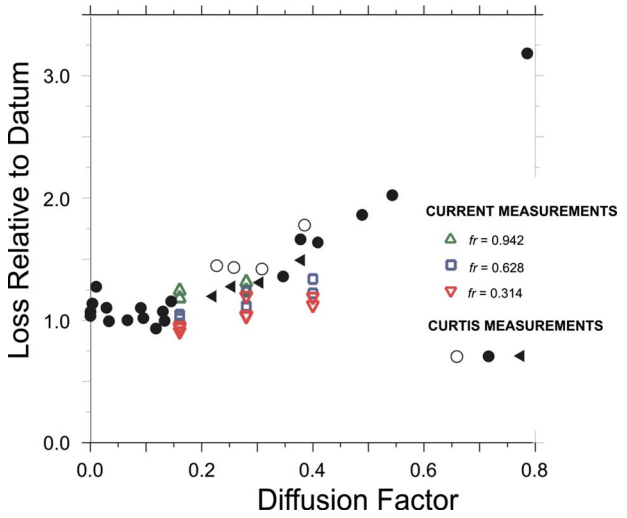

Fig. 11 Relative loss versus diffusion factor for current measurements and those of Curtis et al. [3] at Re_c=200,000.

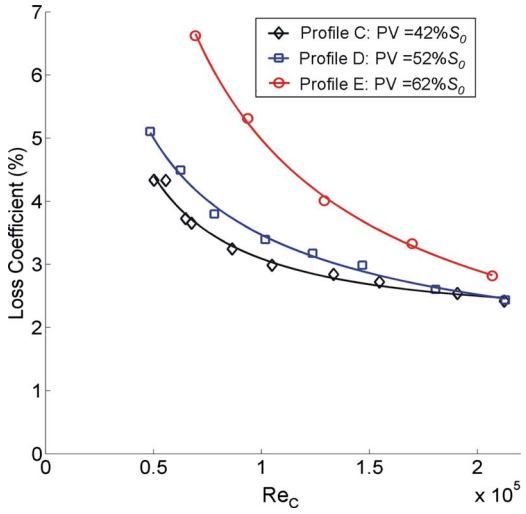

Fig. 12 Influence of varying peak velocity location. Loss for designs C–E (DF=28%) at f_r=0.314.

freestream turbulence level was 0.5% compared with 3% in the current study and the unsteady reduced frequency was set at 1.5, slightly higher than the range of the current study (0.314–0.942).

Figure 11 shows a plot of relative suction surface loss against diffusion factor from Curtis et al. [3] at Re_c=200,000, overlaid with the results from the current study. The data from Curtis et al. [3] show that loss increases sharply with diffusion factor above a value of approximately 0.2. The current results show the same overall trend but also a variation with reduced frequency. The lowest reduced frequency cases (f_r=0.314 and f_r=0.628) exhibit lower loss than the other cases, while the current measurements at f_r=0.942 (the closest value to the configuration of Curtis et al. [3]) fall within the range of the previous measurements.

3.3.2 Variation of Peak Velocity Location. To design a blade for unsteady flow conditions, it is desirable to know how far forward or aft on the surface to locate the peak velocity in order to minimize loss production. Once again, the steady flow behavior of the boundary layers is a useful starting point for comparisons. Table 5 summarizes the proportions of laminar, separated, and turbulent flows for the three designs with a 28% diffusion factor (C–E) under steady flow conditions. The average non-dimensional deceleration rate is again presented in the final column.

Moving the peak velocity aft on the blade increases the deceleration rate (Eq. (11)) but reduces the length of the turbulent boundary layer. This will tend to increase the bubble-generated losses (which dominate the overall loss at low Reynolds numbers) yet decrease the losses produced in the turbulent boundary layer (which dominate at high Reynolds numbers). Therefore, moving the peak velocity location further aft will tend to improve high Reynolds number performance at the expense of low Reynolds number performance. Evidence of this trade-off can be seen in the loss measurements.

Table 5 Approximate proportion of laminar, separated, and turbulent flows across blade surfaces for the DF=28% designs at Re_c≈125,000

Design name	Peak velocity location ($\%S_0$)	Surface distances: Laminar attached ($\%S_0$)	Surface distances: Length of bubble ($\%S_0$)	Surface distances: Turbulent attached ($\%S_0$)	Average deceleration rate[a]
C	42	54	25	21	0.48
D	52	59	24	17	0.58
E	62	68	20	12	0.74

[a]Equation (11).

Figure 12 shows the measured loss coefficient for designs C–E for the lowest reduced frequency (f_r=0.314). Design C, with the lowest rate of diffusion, clearly outperforms the other distributions up to Re_c=200,000. At this Reynolds number, designs C and D have the same loss, but the gradients perhaps suggest that design D will outperform design C at higher Reynolds numbers. This suggested "crossover" in performance is in line with the trends observed by the authors when varying the peak velocity at different diffusion factors and reduced frequencies.

Design E has the highest deceleration rate and performs poorly compared with the other two designs across the Reynolds number range. This is in part because this design has relatively low lift as a result of the reduced leading edge loading and hence has a pitch-to-chord ratio that is approximately 8% below the other designs (as listed in Table 2). This directly influences the calculated loss (as Eq. (8) shows) but at most accounts for only an 8% increase. The increase in loss evident in Fig. 12 for profile E is greater than 8% of the measured loss of designs C and D across the whole Reynolds number range and is, in fact, approaching 70% at Re_c=70,000. The high loss for design E is therefore primarily due to the high bubble-generated losses in the more severely diffusing flow.

Figures 13 and 14 can be used to compare the unsteady boundary layer behavior of designs C and E, respectively, for f_r=0.628 and Re_c≈130,000. The phase-averaged quasiwall shear stress has been plotted as flood contours on a space-time diagram, with line contours of intermittency (in steps of 0.1) superimposed. The white dots at the top of each plot again indicate the streamwise positions of the hot-film sensors. As for Fig. 4, lines indicating the approximate regions influenced by the wakes have been added. Illustrations have been drawn above and below to highlight the boundary layer behavior. Labels locate the positions of the peak velocity, separation, and turbulent reattachment. Regions of unsteady separation are visible as areas of low quasi-wall shear stress, downstream of which the boundary layer undergoes transition (indicated by the rising intermittency contours) and reattachment (indicated by high quasi-wall shear stress values).

Figure 13 shows the results for design C, which has the peak velocity located at 42%S_0. The laminar boundary layer separates at 54%S_0. This is followed by turbulent reattachment at around 79%S_0 for those periods between the wakes. Underneath the wakes, however, reattachment occurs at around 68%S_0. Due to the

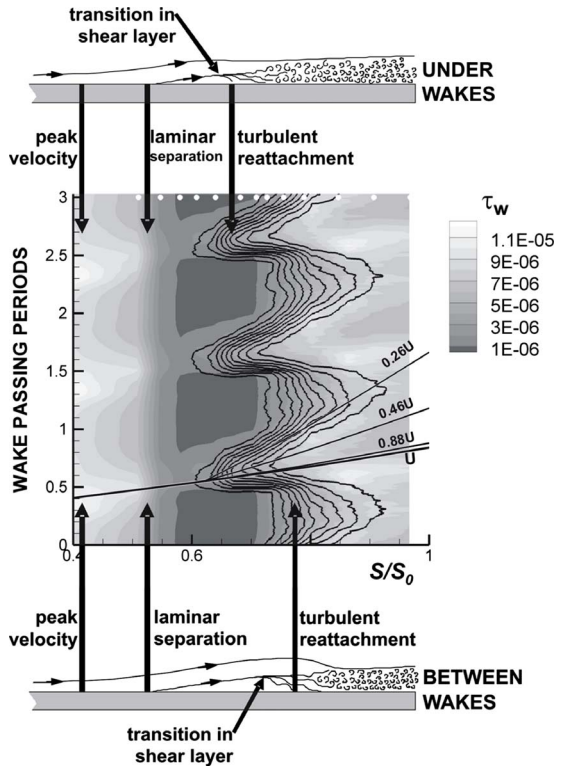

Fig. 13 Flood contours of quasi-wall shear stress and line contours of intermittency (in steps of 0.1) for design C (DF =28%, S_{peak}/S_0=42%, Re_c=130,000, and f_r=0.628)

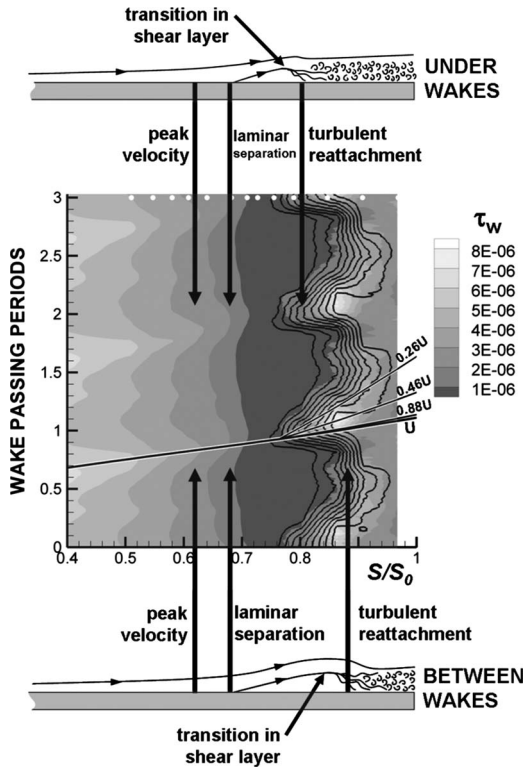

Fig. 14 Flood contours of quasi-wall shear stress and line contours of intermittency (in steps of 0.1) for design E (DF =28%, S_{peak}/S_0=62%, Re_c=138,000, and f_r=0.628)

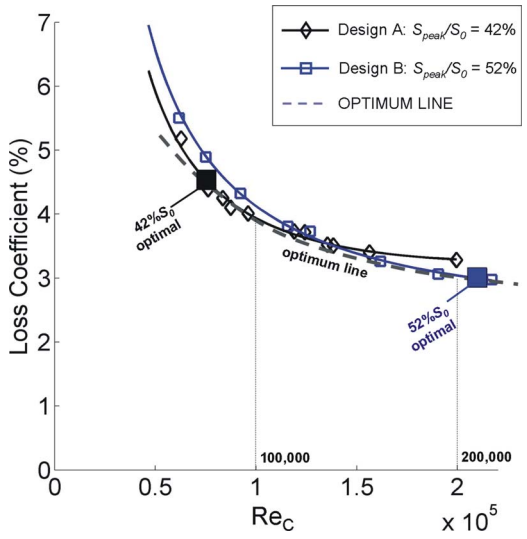

Fig. 15 Influence of varying peak velocity location. Loss coefficients for designs A and B (DF=40%) at f_r=0.628 with optimum line. Approximate optimum peak velocity locations have been added.

unsteady nature, transition and reattachment can begin as early as 60%S_0 (effectively closing the bubble) or as late as 75%S_0. This variation is evident in the raw traces of the hot-film data, which are not presented here.

Figure 14 shows the results for design E with the peak velocity located at 62%S_0. The laminar boundary layer remains attached until separation at 68%S_0. As demonstrated by the illustration below the figure, turbulent reattachment occurs between the wakes at approximately 88%S_0. Directly underneath each wake, however, reattachment occurs around 80%S_0, as demonstrated by the illustration above the figure. The raw hot-film traces show that transition rarely moves further upstream than 75%S_0, indicating that the bubble is never entirely suppressed in this case. It can therefore be inferred that the separation bubble is somewhat more robust for design E than design C due to the high diffusion rate. As was observed for the steady flow data in Table 5, under unsteady flow conditions, design C, having a peak velocity forward on the surface, has a greater extent of turbulent boundary layer flow than design E. It also has a less robust separation bubble.

3.4 Optimum Designs. The effects of diffusion factor, peak velocity location, and reduced frequency on the loss trends have been discussed individually, but the more complicated issue of how their effects combine must still be dealt with. The main barrier to presenting this information is the large amount of data that needs to be compared simultaneously. To avoid plotting a large number of loss trends on a single figure for direct comparison, the authors will focus on what are considered to be the "optimum" designs as suggested by the measurements. It should, however, be noted that this discussion applies only to the eight profiles studied. The effects of increased or decreased leading edge loading, which will affect the loss as well as the incidence tolerance, are outside the scope of this study.

Figure 15 presents measured loss for the 40% diffusion factor designs A and B, plotted for a reduced frequency of 0.628. In a similar manner to the trends observed in Fig. 12, there is evidence of a trade-off when moving the peak velocity location. Design A, with the lowest rate of diffusion, outperforms design B below a Reynolds number of Re_c=120,000 because it has lower bubble-generated losses. Above this cross-over point, design B has a better performance because it has a shorter extent of turbulent boundary layer flow.

An optimum line has been added to the plot, representing the

minimum loss achievable by moving only the peak velocity location and keeping the reduced frequency and diffusion factor constant. The points at which the loss coefficient curves coincide with the optimum curve have been marked on the figure. These represent the Reynolds numbers at which the two designs are optimal. Interpolation between these points allows estimates to be made of the optimum peak velocity location and profile loss for a given Reynolds number. The optimum line shows the same result as the individual loss trends for each design, namely, that as the Reynolds number increases, peak velocity should be moved aft on the surface to minimize loss. For example, at $Re_c = 100{,}000$, the suggested optimum peak velocity location is around $44\%S_0$, close to that of design A. An increase in Reynolds number favors a further aft peak velocity and hence at $Re_c = 200{,}000$, the estimated optimum peak velocity location is around $51\%S_0$, closer to design B.

3.5 Variation of Diffusion Factor and Peak Velocity Location. Figure 16(*b*) shows the optimum lines, similar to that drawn in Fig. 15, for all three diffusion factors at a reduced frequency $f_r = 0.628$. Data obtained from the loss measurements of all eight designs have been used to produce this plot. The measured loss curves have been omitted for clarity. Again the approximate optimum conditions for each peak velocity location have been added. The optimum lines in Fig. 16(*b*) show the same trends observed in the previous results. At low Reynolds numbers ($Re_c \approx 50{,}000$), the optimum peak velocity location is close to $42\%S_0$. This is consistent with the previous discussion of the peak velocity location (see Figs. 12 and 15), where it was observed that such designs had the lowest loss at low Reynolds numbers. Conversely as the Reynolds number increases, Fig. 16(*b*) shows that in general moving the peak velocity location aft is desirable to obtain minimum loss, again in line with earlier observations.

As seen in Fig. 9, Fig. 16(*b*) also shows that the loss rises with increasing diffusion factor across the whole Reynolds number range. Thus for well-designed blades, the loss generated is primarily determined by the diffusion factor. The increase in loss with diffusion factor becomes more severe at low Reynolds numbers due to the rapid increase in bubble-generated losses for high diffusion factor designs (as shown in Fig. 10).

Figure 16(*b*) also shows the effect of diffusion factor on the optimal peak velocity location. This can be estimated by interpolating between the $42\%S_0$ and $52\%S_0$ optimum points. For $Re_c = 120{,}000$, the peak velocity locations listed in Table 6 are approximately optimal.

As the diffusion factor increases, it becomes more favorable to move the peak velocity forward to reduce the rate of diffusion and hence the bubble-generated mixing loss. This implies that while both the bubble-generated and turbulence-generated losses rise with increasing diffusion factor, the increase in bubble-generated loss dominates the trend. This agrees with the comparisons made with the laminar and turbulent loss trends in Fig. 9. As the diffusion factor increases, the loss measurements follow an increasingly laminar trend, suggesting that loss produced by the bubble dominates over the losses generated in the turbulent boundary layer downstream of reattachment.

As discussed previously, a decrease in reduced frequency increases the bubble-generated losses. It therefore becomes more favorable to move the peak velocity forward to offset the increased bubble losses. This trend can be observed by comparing the optimum plots of Figs. 16(*a*) and 16(*b*), which show the optimum lines for the low (0.314) and high (0.942) reduced frequencies, respectively.[4] Table 7 compares the optimum peak velocity locations of the 28% diffusion factor designs for the three reduced frequencies at $Re_c = 120{,}000$. This confirms that the peak velocity should move forward with decreasing reduced frequency to mitigate the increased bubble loss.

[4]Not all of the designs were tested at the highest reduced frequency; hence there is no optimum line for the 40% diffusion factor designs in Fig. 16(*c*).

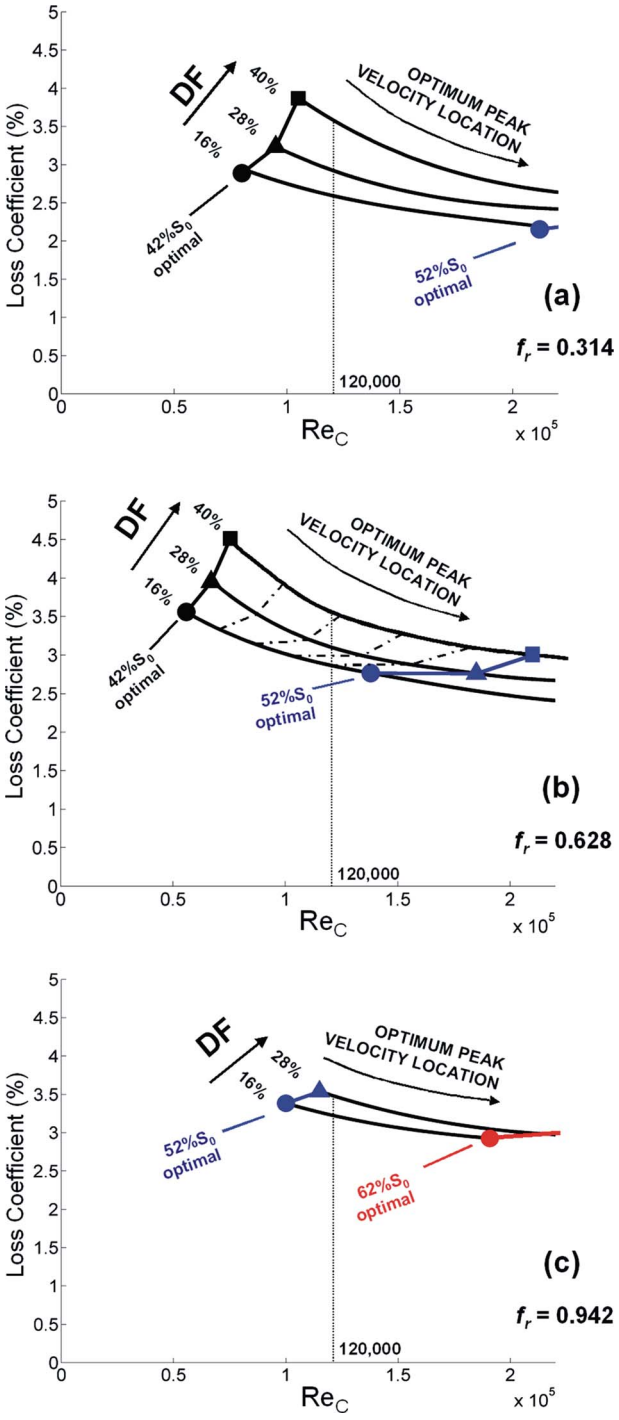

Fig. 16 Optimum lines and approximate optimum peak suction locations for each diffusion factor. (*a*) $f_r = 0.314$, (*b*) $f_r = 0.628$, and (*c*) $f_r = 0.942$.

4 Conclusions

The results presented in this paper have shown that a sensitive balance exists between separation bubble-generated losses and reattached turbulent losses in the suction surface boundary layers of high-lift LP turbine blades.

Measurements presented for a single design (DF=28%, PV $= 52\%S_0$) have shown that the overall losses follow a laminar trend ($Re_c^{-0.5}$) at low Reynolds numbers and follow a turbulent trend ($Re_c^{-0.2}$) at higher Reynolds numbers. This indicates that in the low Reynolds number regime, the large suction-side separa-

Table 6 Optimal peak velocity locations for $f_r=0.628$ and $Re_c=120{,}000$

Diffusion factor (%)	Optimal peak velocity location ($\%S_0$)
16	50
28	45
40	44

tion bubble governs the overall loss production, while at high Reynolds numbers, the bubble is small and the loss generated in the turbulent boundary layer downstream of reattachment dominates.

The introduction of unsteady wakes had the effect of periodically suppressing the streamwise extent of the separation bubble while introducing high-loss turbulent regions, which arrive at the trailing edge just behind each wake. The effect on the overall loss is governed by the balance between the bubble-generated losses and the high-loss turbulent regions. At high Reynolds numbers, when bubble-generated losses are low, the introduction of unsteady wakes increases loss production. Increasing the reduced frequency further increases the fraction of the wake passing period occupied by the high-loss turbulent region. Conversely at low Reynolds numbers, when separation-generated losses tend to dominate the overall loss production, the introduction of unsteady wakes beneficially suppresses the separation causing a reduction in the boundary layer loss. Increasing the reduced frequency tends to reduce the loss further.

A study of eight velocity distribution designs has shown that the loss increases with the diffusion factor throughout the Reynolds number range. Comparing the results with a non-separated boundary layer calculation shows that the bubble-generated losses increase significantly with diffusion factor at low Reynolds numbers. Hot-film measurements also show that transition moves upstream with increasing diffusion factor, leading to a larger extent of turbulent boundary layer flow and increased loss.

For a given diffusion factor, moving the peak velocity forward on the surface reduces the diffusion rate. This tends to reduce the bubble-generated losses, at the cost of increasing the extent of the turbulent boundary layer. Front-loading therefore improves the low Reynolds number performance, where bubble-generated losses are more significant, at the expense of the high Reynolds number performance, where turbulence-generated losses are more dominant. Conversely, moving the peak velocity further aft has the opposite impact, reducing loss at high Reynolds numbers at the expense of low Reynolds number performance.

The measurements have shown that an optimum exists as to the location of the peak velocity. This interdependent relationship varies with Reynolds number, diffusion factor, and reduced frequency. Charts illustrating the relationship between peak suction location, diffusion factor, and boundary layer loss across a range of Reynolds numbers have been plotted for three reduced frequencies. At its simplest, reducing the rate of diffusion will tend to reduce the bubble-generated losses. In general, this is more beneficial with decreasing Reynolds number, decreasing reduced frequency, and for higher diffusion factor designs.

For well-designed distributions (with peak velocities locations close to the optimum locations), the loss is primarily a function of the diffusion factor.

Table 7 Optimal peak velocity locations for DF=28% and $Re_c=120{,}000$[a]

Reduced frequency	Optimal peak velocity location ($\%S_0$)
0.314	44
0.628	45
0.942	53

[a]These are approximate values because the optimum conditions for some of the designs lie outside the measured Reynolds number range.

Acknowledgment

The authors would like to thank EPSRC and Rolls-Royce for funding the research project. Thanks also are due to Whittle Laboratory technical staff, Greg Walker of the University of Tasmania, and Rolls-Royce for their assistance and technical guidance.

Nomenclature

Symbols

C = equivalent chord
C_x = equivalent axial chord
C_{pb} = base pressure coefficient
E = hot-film bridge output voltage
E_0 = hot-film bridge zero-flow output voltage
f_{bar} = Bar Passing Frequency
f_r = reduced frequency $=(f_{bar}C/U_{TE})$
$R(\tau)$ = autocorrelation function $=\lim_{T\to\infty}\int_{-\infty}^{\infty}x(t)x(t+\tau)dt$
Re_c = chord-based Reynolds number $=(U_{TE}C/\nu)$
Re_{S0} = surface length-based Reynolds number $=(US_0/\nu)$
s = pitch
S = surface distance from leading edge
S_{peak} = peak velocity location
ΔS = length of decelerating region $=(S_0-S_{peak})$
S_0 = total surface length
t = equivalent trailing edge thickness
t_r = residence time
u = measured velocity of LDA bursts
$\langle u\rangle$ = phase-averaged velocity
U = local freestream velocity
U_{TE} = trailing edge freestream velocity
U_{max} = maximum freestream velocity
ΔU = total deceleration $=U_{max}-U_{TE}$
Z = Zweifel lift coefficient (Eq. (7))
α_1 = inlet angle
α_2 = exit angle
δ^* = displacement thickness
ζ = suction surface loss coefficient (Eq. (8))
θ = momentum thickness
Λ = turbulence integral length scale
η = residence time weighting factor
ν = kinematic viscosity
τ_w = quasiwall shear stress

Abbreviations

DF = diffusion factor $=((U_{max}-U_{TE})/U_{TE})$

References

[1] Halstead, D. E., 1996, "Boundary Layer Development in Multi-Stage Low Pressure Turbines," Ph.D. thesis, Iowa State University, Ames, IA.
[2] Halstead, D. E., Wisler, D. C., Okiishi, T. H., Walker, G. J., Hodson, H. P., and Shin, H. W., 1997, "Boundary Layer Development in Axial Compressors and Turbines: Part 3 of 4—LP Turbines," ASME J. Turbomach., **119**, pp. 225–237.
[3] Curtis, E. M., Hodson, H. P., Banieghbal, M. R., Howell, R. J., and Harvey, N. W., 1997, "Development of Blade Profiles for Low-Pressure Turbine Applications," ASME J. Turbomach., **119**, pp. 531–538.
[4] Sharma, O. P., Wells, R. A., Schlinker, R. H., and Bailey, D. A., 1982, "Boundary Layer Development on Turbine Suction Surfaces," ASME Paper No. 81-GT-204, pp. 698–706.
[5] Howell, R. J., Ramesh, O. N., Hodson, H. P., Harvey, N. W., and Schulte, V., 2001, "High Lift and Aft-Loaded Pressure Profiles for Low-Pressure Turbines," ASME J. Turbomach., **123**, pp. 181–188.

[6] Pfeil, H., Herbst, R., and Schröder, T., 1982, "Investigations of the Laminar-Turbulent Transition of Boundary Layers Disturbed by Wakes," ASME Paper No. 82-GT-0406.
[7] Stieger, R., and Hodson, H. P., 2004, "The Transition Mechanism of Highly Loaded LP Turbine Blades," ASME J. Turbomach., **126**, pp. 536–543.
[8] Haselbach, F., Schiffer, H. P., Horsman, M., Dressen, S., Harvey, N., and Read, S., 2002, "The Application of Ultra High Lift Blading in the BR715 LP Turbine," ASME J. Turbomach., **124**, pp. 45–51.
[9] Clarke, J. P., and Koch, P. J., 2006, "Designing Turbine Airfoils to Answer Research Questions in Unsteady Aerodynamics," Minnowbrook V 2006 Workshop on Unsteady Flows in Turbomachinery, Paper No. NASA/CP-2006-214484.
[10] Bons, J., 2006, "Unsteady Transition and Separation in an LPT Cascade," Minnowbrook V 2006 Workshop on Unsteady Flows in Turbomachinery, Paper No. NASA/CP-2006-214484.
[11] Opoka, M. M., and Hodson, H. P., 2007, "Transition on the T106 LP Turbine Blade in the Presence of Moving Upstream Wakes and Downstream Potential Fields," ASME Paper No. GT2007-28077.
[12] Zhang, X. F., and Hodson, H. P., 2007, "Effects of Reynolds Number and Freestream Turbulence Intensity on the Unsteady Boundary Layer Development on an Ultra-High-Lift LPT Airfoil," ASME Paper No. GT2007-27274.
[13] Stieger, R. D., 2002, "The Effects of Wakes on Separating Boundary Layers in Low-Pressure Turbines," Ph.D. thesis, University of Cambridge, Cambridge, England.
[14] Opoka, M. M., Thomas, R. L., and Hodson, H. P., 2006, "Boundary Layer Transition on the High Lift T106A LP Turbine Blade With an Oscillating Downstream Pressure Field," ASME Paper No. GT2006-91038.
[15] Zhang, X. F., 2005, "Separation and Transition Control on Ultra-High-Lift Low Pressure Turbine Blades in Unsteady Flow," Ph.D. thesis, University of Cambridge, Cambridge, England.
[16] George, W. K., 1975 "Limitations to Measuring Accuracy Inherent in the Laser-Doppler Signal," *Proceedings of the LDA Symposium*, Copenhagen, Denmark.
[17] Hodson, H. P., 1983, "The Detection of Boundary Layer Transition and Separation in High Speed Turbine Cascades," *Proceedings of the Seventh Symposium on Measurement Techniques for Transonic and Supersonic Flow*, Aachen, Germany, Sept. 21–23.
[18] Denton, J. D., 1993, "*The 1993 IGTI Scholar Lecture:* Loss Mechanisms in Turbomachines," ASME J. Turbomach., **115**, pp. 621–656.
[19] Roberts, Q. D. H., 1997, "The Trailing Edge Loss of Subsonic Turbine Blades," Ph.D. thesis, University of Cambridge, Cambridge, England.
[20] Solomon, W. J., 1996 "Unsteady Boundary Layer Transition on Axial Compressor Blades," Ph.D. thesis, University of Tasmania, Tasmania, Australia.
[21] Herbert, M. V., and Calvert, W. J., 1982, "Description of an Integral Method for Calculation in Use at NGTE, With Special Reference to Compressor Blades," NGTE Memorandum No. M82019.
[22] Abu-Ghannam, B. J., and Shaw, R., 1980, "Natural Transition of Boundary Layers—The Effect of Turbulence, Pressure Gradient, and Flow History," J. Mech. Eng. Sci., **22**(5), pp. 213–228.
[23] Horton, H. P., 1967, "A Semi-Empirical Method for the Growth and Bursting of Laminar Separation Bubbles," ARC Paper No. CP1073.
[24] Green, J. E., Weeks, D. J., and Brooman, J. W. F., 1977, "Predictions of Turbulent Boundary Layers in Compressible Flow by a Lag-Entrainment Method," ARC R&M Paper No. 3791.
[25] Gostelow, J. P., Melwani, N., and Walker, G. J., 1996, "Effects of Streamwise Pressure Gradient on Turbulent Spot Development," ASME J. Turbomach., **118**, pp. 737–743.
[26] Hodson, H. P., 1990, "Modelling Unsteady Transition and Its Effects on Profile Loss," ASME J. Turbomach., **112**, pp. 691–701.
[27] Lazaro, B. J., Gonzalez, E., and Vazquez, R., 2007,"Unsteady Loss Production Mechanisms in Low Reynolds Number, High Lift, Low Pressure Turbine Profiles," ASME Paper No. GT2007-28142.
[28] Hourmouziadis, J., and Hofmann, G., 2006, "Response of Separation Bubble to Velocity and Turbulence Wakes," Minnowbrooke VI Proceedings, Paper No. NASA/CP-2006-214484.
[29] Schlichting, H., 1979, *Boundary Layer Theory*, 7th ed., McGraw-Hill, New York.